Journal of Electroceramics
https://doi.org/10.1007/s10832-026-00467-8

Optimal La^{3+} window in $Pb_{1-x}La_xTiO_3$: balancing structural, microstructural, dielectric, and optical properties

Fernando A. Londoño Badillo[1] · Lucas Sierra[1] · Jesús Vega-Castillo[2,3] · José Antonio Eiras[4] · Ducinei Garcia[4]

Received: 17 September 2025 / Accepted: 28 February 2026

Abstract
Obtaining transparent ferroelectric ceramics requires balancing electrical and optical properties, typically achieved through controlled doping. In this study, densified lead titanate (PT) ceramics doped with different concentrations of lanthanum (PLT18, PLT20, and PLT22) were synthesized and characterized structurally, dielectrically, and optically. All compositions crystallized in a tetragonal perovskite structure; with increasing lanthanum content, the Curie temperature decreased and the diffuseness exponent (γ) increased, indicating a progressively more diffuse transition. Despite these trends, the maximum permittivity remained high and the dielectric loss was generally low. Among the compositions studied, PLT20 defined an optimal window for combined electrical and optical performance: it attained ~ 40% transmittance at 650 nm while exhibiting reduced influence of ferroelectric domain activity under operating conditions and a minimal contribution from secondary phases relative to adjacent compositions. This combination yields stable dielectric behavior with moderate loss and supports reliable electro-optic functionality. Collectively, the structural, dielectric, and optical results for the PLT20 ceramic establish it as a practical composition for lead-based transparent ferroelectric components.

Keywords Transparent PLT ceramics · Electro-optic coefficients · Lanthanum-doped lead titanate · Dielectric permittivity · Rietveld refinement

1 Introduction

Ferroelectric materials have played a crucial role in scientific and technological advancements over the decades. Their unique combination of high dielectric constant, remarkable piezoelectric properties, and significant electrostriction has made them indispensable in a wide range of applications, from capacitors and sensors to actuators and memory devices [1]. Historically, lead-based ferroelectric ceramics, such as $Pb(Zr,Ti)O_3$ (PZT) and $Pb(Mg_{1/3}Nb_{2/3})O_3$–$PbTiO_3$ (PMN-PT), have been at the forefront of this field, driving innovations in electronics, medical imaging, and energy harvesting technologies. The continuous development and optimization of these materials have enabled the miniaturization and enhanced performance of electronic devices, while ongoing research into lead-free alternatives and sustainable processing methods reflects the field's adaptation to environmental and health concerns. As a result, ferroelectric materials remain vital for next-generation smart devices and energy solutions, underscoring their enduring importance in modern science and industry [1, 2].

As regards, lanthanum doping in lead titanate ($PbTiO_3$) ceramics, especially in hot-pressed samples, substantially modifies and often enhances their properties by introducing A-site vacancies ($Pb_{1-1.5x}La_xTiO_3$), which modifies electrical, optical, and electro-optic behavior [3]. Electrically, La^{3+} substitution reduces tetragonality and linearly depresses the Curie temperature (Tc), while optimizing dielectric properties [4]. Optically, La doping enhances both optical and electro-optic effects, including electric-field-dependent refractive index modulation. These synergistic

✉ Fernando A. Londoño Badillo
fernandoa.londono@udea.edu.co

1 Facultad de Ciencias Exactas y Naturales, Universidad de Antioquia, UdeA, Calle 70 No. 52-21, Medellín, Colombia

2 YPF Tecnología, Provincia de Buenos Aires, Berisso, Argentina

3 Consejo Nacional de Investigaciones Científicas y Técnicas CONICET, Godoy Cruz 2290, C1425FQB Buenos Aires, Argentina

4 Grupo de Materiais Ferroicos – Universidade Federal de São Carlos, São Carlos, Brasil

Published online: 17 March 2026

improvements position La-doped $PbTiO_3$ as a versatile platform for advanced optoelectronic devices [3]

As mentioned, lanthanum doping in lead titanate (PLT) ceramics (particularly in hot-pressed ceramics) alters structural and functional properties by substituting La^{3+} for Pb^{2+} at A sites, thereby reducing tetragonality (c/a) and mitigating the internal stresses that cause microcracking in pure $PbTiO_3$. At low doping levels ($x \leq 0.10$), La^{3+} incorporation creates A-site vacancies, leading to a near-linear decrease in tetragonality and Curie temperature (Tc) while increasing permittivity [5, 6]. At high lanthanum concentrations ($x \geq 0.30$), the structure approaches cubic symmetry ($c/a \approx 1.000$), relieving internal stress but sacrificing ferroelectricity [4]. Consequently, most studies have focused on these compositional extremes, leaving a critical gap in the intermediate range. This intermediate window in conventionally processed ferroelectric PLT ceramics remains sparsely explored; addressing it enables a systematic correlation between lanthanum content, grain growth and domain structure, and the resulting dielectric, optic and electro-optic properties.

Moreover, most previous studies on PLT ceramics have relied on direct Rietveld refinement of the full diffraction profile without an initial profile-decomposition step. This practice can obscure minor secondary phases and bias the determination of unit cell parameters particularly under severe peak overlap underscoring the need for complementary approaches to Rietveld refinement, such as the Le Bail method, to ensure reliable structural characterization [5, 6].

The Le Bail method, a whole-pattern decomposition approach, enables structureless refinement of powder diffraction data by iteratively distributing observed intensities among overlapping reflections without imposing atomic coordinate constraints [7]. Although successfully applied to various oxides, this approach has not been systematically extended to lanthanum modified lead titanate (PLT) ceramics, particularly within the intermediate composition window ($Pb_{1-x}La_xTiO_3$, $0.18 < x < 0.22$), where hot-pressed PLT often exhibits a balanced dielectric and electro-optic response, while comparable studies on conventionally sintered ceramics are lacking [5, 8]. Our innovative work addresses this gap by first employing Le Bail decomposition to isolate phase contributions and validate phase purity, followed by Rietveld refinement.

In this work, we systematically investigate ferroelectric $Pb_{1-x}La_xTiO_3$ (PLTX) ceramics produced by conventional pressureless sintering within the underexplored intermediate La^{3+} doping window ($x = 0.18$, 0.20, 0.22). Structural parameters are quantified by coupling whole-pattern profile decomposition (Le Bail) with subsequent Rietveld refinement, enabling rigorous determination of lattice parameter and minor secondary phases. These results are integrated with microstructural analysis (grain-size, grain-boundary character/density, ferroelectric domain), optical (visible transmittance), dielectric (permittivity, loss tangent), and electro-optic measurements (Pockels/Kerr coefficients). The objective of this work is to establish quantitative composition–microstructure–property correlations and to elucidate how compositional variations, grain size, grain-boundary characteristics, and ferroelectric domain structure jointly govern the structural, optical, dielectric, and electro-optic responses of conventionally sintered PLT ceramics, thereby validating the lanthanum concentration window proposed here as optimal for PLT transparent electric applications.

2 Experimental procedure

Precursors including lead oxide (PbO, 99.3% purity, Aldrich), titanium dioxide (TiO_2, 99.7% purity, Aldrich), and lanthanum oxide (La_2O_3, 99.9% purity, Alfa Aesar) were used to synthesize $Pb_{(1-1.5x)}La_xTiO_3$, (PLTx) ceramics. An excess of lead, corresponding to the stoichiometry $Pb_{(1-x)}La_xTiO_3$, was added, resulting in an average lead excess of 15%. Powders were prepared with compositions where $x = 0.18$ (PLT18), $x = 0.20$ (PLT20), and $x = 0.22$ (PLT22). The powders were weighed, mixed for 3 h, with ethanol as the solvent and zirconia cylinders as the milling media.

The mixed powders were calcined at 850 °C for 3 h in an air atmosphere. The resulting material was shaped into discs with a diameter of 14 mm and a thickness of 2 mm. The samples were densified in a conventional furnace at different temperatures and holding times, following the setup shown in Fig. 1. The optimal densification conditions for PLT18 and PLT20 were found to be 1180 °C for 3 h, whereas for the PLT22 sample, the optimal condition was 1220 °C for 6 h. After densification process, the ceramic surfaces were polished, and post-sintering thermal treatments were performed in lead and oxygen rich atmospheres to minimize lead volatilization and formation of oxygen vacancies. The system used for these processes is shown in Fig. 1. The treatments were conducted for 5 h at 1000 °C. Post-sintering treatments in oxygen and lead rich atmospheres were performed with the aim of enhancing the transparency of the ceramic. Figure 1 illustrates the system employed to prevent lead loss and the formation of oxygen vacancies during subsequent treatments, aimed at achieving transparency in the PLT18, PLT20 and PLT22 ceramics. Part (a) of the figure shows the sample to be characterized, positioned between two samples of the same composition to minimize lead losses. Part (b) depicts the sealed system, which utilizes a cement composed of lead and zirconium to further mitigate lead loss. The entire system is placed inside

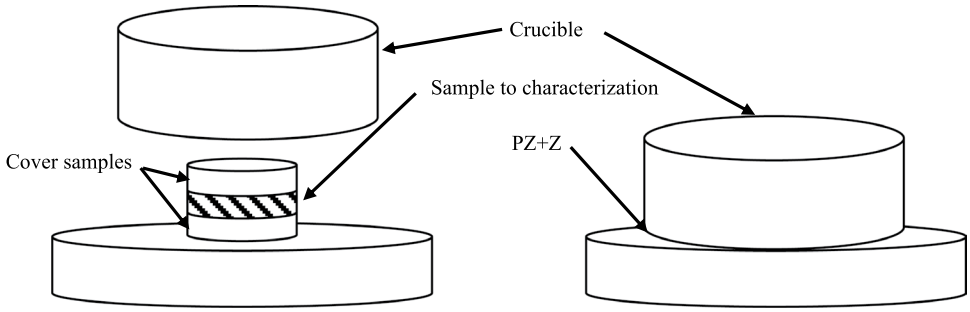

Fig. 1 Sealed crucible setup used for densification/post-annealing in Pb- and O_2-rich atmospheres to suppress lead volatilization: (**a**) prior to sealing with PZ+Z and cover pellets; (**b**) sealed configuration

a furnace with rich oxygen atmosphere. A similar scheme was designed to control lead and oxygen loss in lead zirconate titanate ceramics [9].

The relative densities of the ceramics were measured using the Archimedes method. The fracture microstructure was analyzed via scanning electron microscopy (SEM), and grain sizes were determined using the linear intercept method [10]. Structural properties were characterized at room temperature using X-ray diffraction (XRD), with phase identification and lattice parameter refinement performed through the Le Bail and Rietveld methods [11, 12]. Relative permittivity, were evaluated using impedance analysis with an HP4194A impedance analyzer. The optical transmittance was determined using a Micronal B582 spectrophotometer that had been adapted for analysis of solid samples. Finally, the transverse electro-optic response was measured at $\lambda = 632.8$ nm using a He–Ne laser and crossed polarizers. The electric field was applied across transparent and optically polished PLT ceramics (~200 µm thick). From the measured field-induced birefringence, Δn, the electro-optical coefficients were determined by fitting the Eq. (1) [3]:

$$\Delta n = -\frac{1}{2} n^3 \left(RE^2 + rE\right) \tag{1}$$

where n is the refractive index, R and r are the quadratic (Kerr) and linear (Pockels) electro-optical coefficients, respectively, and E is the applied electric field.

3 Results and discussion

Table 1 summarizes the relative densities of the PLT18, PLT20 and PLT22 ceramics at 1180 and 1220 °C for 3 h and 6 h, followed by post-annealing in a Pb-rich oxygen atmosphere (5 h at 1000 °C). The PLT18 and PLT20 compositions attained their highest densification at 1180 °C after a 3 h dwell, whereas PLT22 reached its maximum relative density at 1220 °C for 6 h.

This trend can be rationalized in terms of liquid-phase sintering. Compositions with lower lanthanum contents

Table 1 Relative density of the ceramics as a function of sintering temperature and sintering time

Relative Density			
Sintering temperature	**Ceramics**	**Sintering time**	
		3 h	6 h
1180 °C	PLT18	96.8(2)	95.6(2)
	PLT20	97.8(0)	95.6(2)
1220 °C	PLT22	95.0(2)	97.7(2)

(PLT18 and PLT20) retain a larger fraction of PbO, which forms a transient liquid phase that accelerates mass transport and thereby reduces both the temperature and the dwell time required for full densification [13]. Instead, the PLT22 ceramic, which contains less lead and therefore generates a smaller liquid fraction, demands either longer holding periods or higher firing temperatures to achieve a relative density comparable to those of PLT18 and PLT20. Evidently, the lead and oxygen atmosphere control system proposed in this study effectively prevented significant density losses and improved the density of PLT ceramics compared to values reported in the literature [3].

Figure 2 presents the SEM micrographs of the fracture surfaces of PLT18, PLT20 and PLT22 ceramics sintered at their respective optimized temperatures and times (PLT18, PLT20 at 1180 °C for 3 h and PLT 21 at 1220 °C for 6 h) with posterior thermal treatment at 1000 °C for 5 h. The microstructures reveal the formation of homogeneous grains with relatively uniform grain sizes, determined by the linear intercept method (not shown here) to be approximately PLT18: (2.0±0.2) µm, PLT20: (2.6±0.2) µm, and PLT22: (3.1±0.2) µm. All samples exhibit a certain degree of porosity, which is consistent with the density values reported in Table 1 when compared to hot-pressed ceramics which have low porosity due to the pressure applied during sintering [4]. In addition, a progressive increase in transgranular fracture is observed with increasing lanthanum content. This behavior suggests a tendency toward increased grain-boundary cohesion, attributable to the reduced PbO content at the grain boundaries with increase of lanthanum [14].

Figure 3 shows the results of the Le Bail refinements performed on the diffraction patterns of PLT18, PLT20, and PLT22 powders calcined at 850 °C for 3 h. The Le Bail

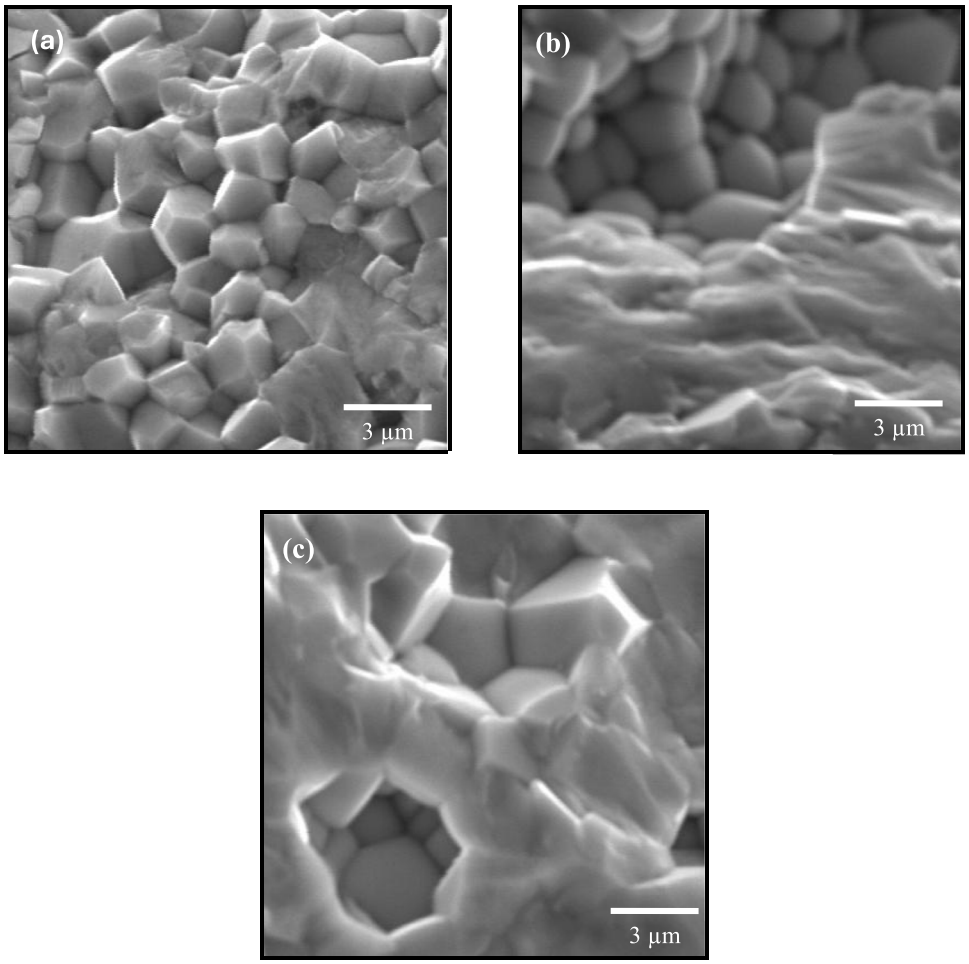

Fig. 2 SEM micrographs of the fracture surfaces of (**a**) PLT18, (**b**) PLT20, and (**c**) PLT22 ceramics sintered at their respective optimized temperatures and times with posterior thermal treatment at 1000 °C for 5 h

refinement is a profile-fitting method that accounts only for the structure factors of the phases involved, without incorporating atomic positional parameters, and is commonly employed as a preliminary step before Rietveld refinement. This approach enables the reliable adjustment of background functions (particularly important for PLT20 and PLT22, where the background exhibited significant irregularities), sample zero-shift (displacement relative to the optical axis), peak-shape functions (in this study modeled using a pseudo-Voigt), and the unit cell parameters of the crystalline phases. In the plots, the red symbols correspond to the experimental data, the black line represents the calculated pattern, the blue line indicates the difference between observed and calculated intensities, and the green marks denote the Bragg reflection positions of the primary phase and the secondary phase. The large number of reflections associated with the monoclinic phase is attributed to its low symmetry. The overall quality of the fits is high, confirming that the refinements are robust and reliable for PLT powders obtained in this work.

The difference line (blue) exhibits only minor deviations (Fig. 3), further supporting the accuracy of the model. A predominant perovskite phase was identified, along with secondary PbO phases arising from the excess lead introduced during the preparation of the ceramic powders. This excess lead was deliberately added to compensate for volatilization losses during the densification process, as previously reported by Guha et al. [15]. The presence of secondary phases in the $Pb_{1-x}La_xTiO_3$ powders is therefore consistent with both the compositional strategy and the approach used to minimize lead loss during thermal treatments. In Fig. 3, most diffraction peaks correspond to the perovskite $PbTiO_3$ structure (COD ID 2107521), while those marked in green are attributed to the monoclinic $La_2Ti_2O_7$ phase (COD ID 1001022), both of which are present at all compositions. The sharp and well-defined reflections confirm the high crystallinity of the material.

Table 2 presents the lattice parameters and tetragonality (c/a) of PLT18, PLT20, and PLT22 powders. The values of a parameter remain nearly constant across all compositions, within experimental uncertainty, indicating that lanthanum substitution does not significantly affect the in-plane lattice dimensions of the perovskite structure. In contrast, the c parameter shows a systematic decrease with increasing

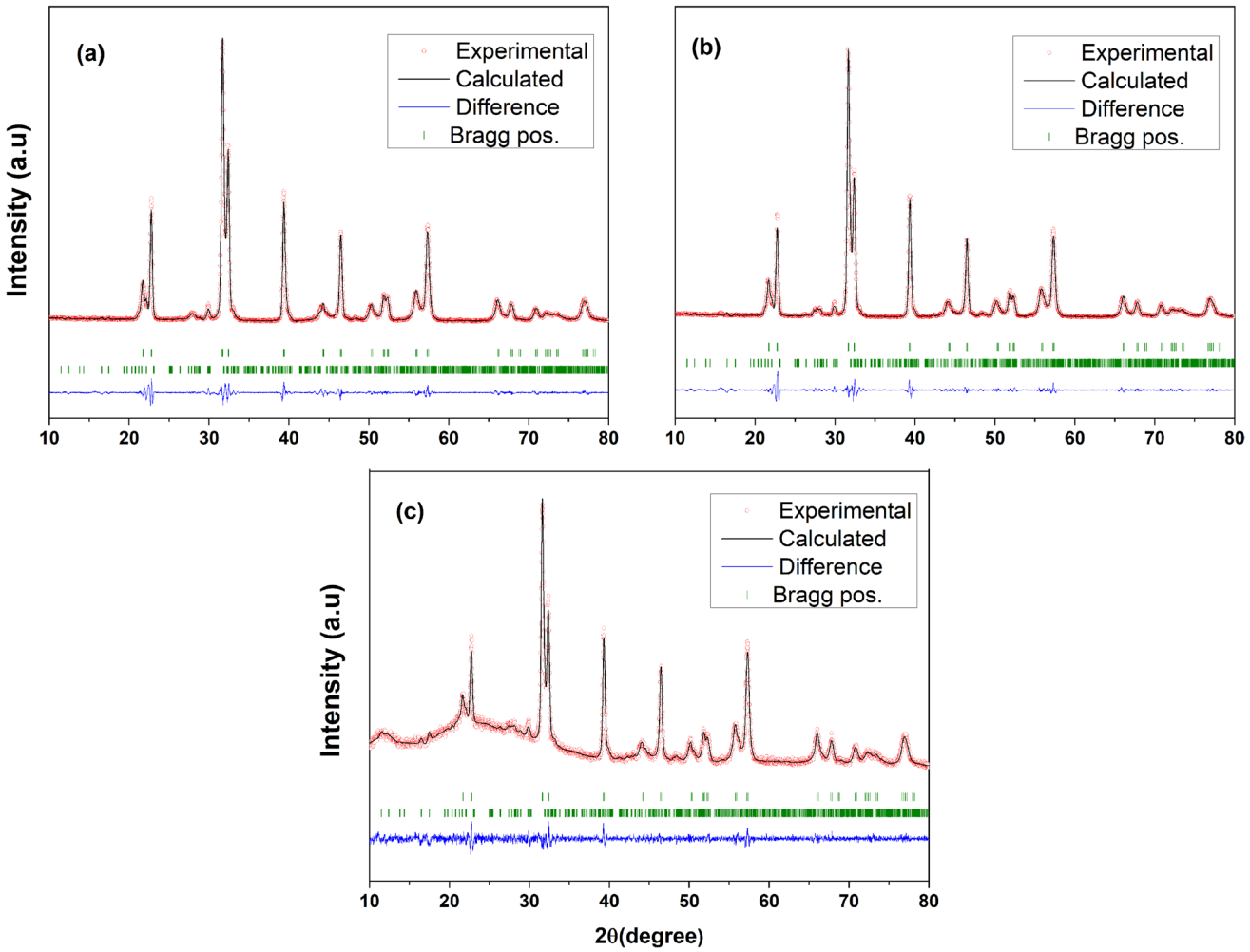

Fig. 3 X-ray diffraction (XRD) patterns of (**a**) PLT18, (**b**) PLT20, and (**c**) PLT22 powders at room temperature, with their refinement

Table 2 Structural parameters and refinement results for PLT18, PLT20 and PLT22 powders obtained from Le Bail and Rietveld refinements

Calcined powder	*a* (Å)	c (Å)	c/ *a* Ratio	%($La_2Ti_2O_7$)	R_{exp}	R_{wp}	R_p	χ^2
PLT18	3.9092(1)	4.0989(1)	1.0485	11.85	5.19	8.69	6.29	2.81
PLT20	3.9076(1)	4.0935(1)	1.0476	13.4	5.17	9.29	6.29	3.22
PLT22	3.9076(1)	4.08457(1)	1.0455	22.56	5.39	6.16	4.83	1.31

La^{3+} concentration. As a result, the tetragonality ratio (*c*/*a*) decreases progressively. This reduction in tetragonal distortion suggests that lanthanum incorporation tends to stabilize a structure closer to the cubic perovskite, thereby reducing the lattice anisotropy. This behavior is consistent with previous reports on La-modified $PbTiO_3$ and related perovskite ceramics, where lanthanum substitution was shown to decrease tetragonal distortion [16].

To estimate the weight fraction of the secondary phase, a Rietveld refinement was carried out using the structural parameters obtained from the previous Le Bail analysis. Unlike the Le Bail method, the Rietveld refinement requires incorporation of the full crystallographic model of the phases, including atomic positions and thermal vibration factors. Since the secondary phase contains 22 distinct atomic positions, the refinement strategy adopted here focused on refining only the crystallographic model of the perovskite phase, while the atomic positions of the $La_2Ti_2O_7$ phase were kept fixed at the values reported in the corresponding crystallographic database.

At the same time, the estimated weight fraction of the secondary $La_2Ti_2O_7$ phase increases markedly with lanthanum. The coexistence of the perovskite phase with an increasing amount of $La_2Ti_2O_7$ reflects the limited solubility of La^{3+} in the $PbTiO_3$ lattice and indicates that, beyond a certain substitution level, lanthanum segregates into this monoclinic secondary phase. The simultaneous decrease in tetragonality and growth of the secondary phase content

highlight the dual structural role of lanthanum, reducing the intrinsic distortion of the perovskite unit cell while favoring the stabilization of $La_2Ti_2O_7$.

The quality of the Rietveld refinement was evaluated through the profile residuals R_p, weighted profile residuals R_{wp}, expected R-factor R_{exp}, and goodness-of-fit χ^2. The R_{wp} values remain below 10% for all compositions, and the reduced chi-squared values (χ^2) range from 3.22 in PLT20 to 1.31 in PLT22. These values indicate a statistically acceptable fit, with PLT22 showing the best agreement between observed and calculated patterns. The relatively stable R_p values (~4.8–6.3%) further confirm the consistency of the profile modeling.

Figure 4 presents the Rietveld refinements of the X-ray diffraction patterns for PLT18, PLT20, and PLT22 ceramics sintered at their respective optimized temperatures and times, each sintered at their respective optimized temperatures and times, and subsequently subjected to post-annealing. In all cases, the experimental data (circles) and calculated profiles (red lines) exhibit excellent overlap, while the difference curves (blue) display residuals low. These results indicate that the structural model used for the perovskite phase is appropriate. Characteristic tetragonal peak splittings of the PLT perovskite are visible and decrease with increasing La^{3+} content, consistent with a reduction in tetragonality (lower *c/a*). A slight shift of reflections to higher 2θ with lanthanum increased is also apparent, in line with lattice contraction expected from La substitution at the A site. These trends are quantified from the Le Rietveld analysis in Table 3. Weak extra reflections, flagged by arrows, are indexed to $La_2Ti_2O_7$ and appear as a minor secondary phase in all compositions. Their relative intensity is smallest for PLT18/PLT20 and becomes more evident in PLT22, which is coherent with the reduced Pb content at higher Lanthanum and the concomitant narrowing of the PbO-rich liquid window during sintering. Overall, the diffraction evidence supports a progressive reduction of tetragonality with lanthanum

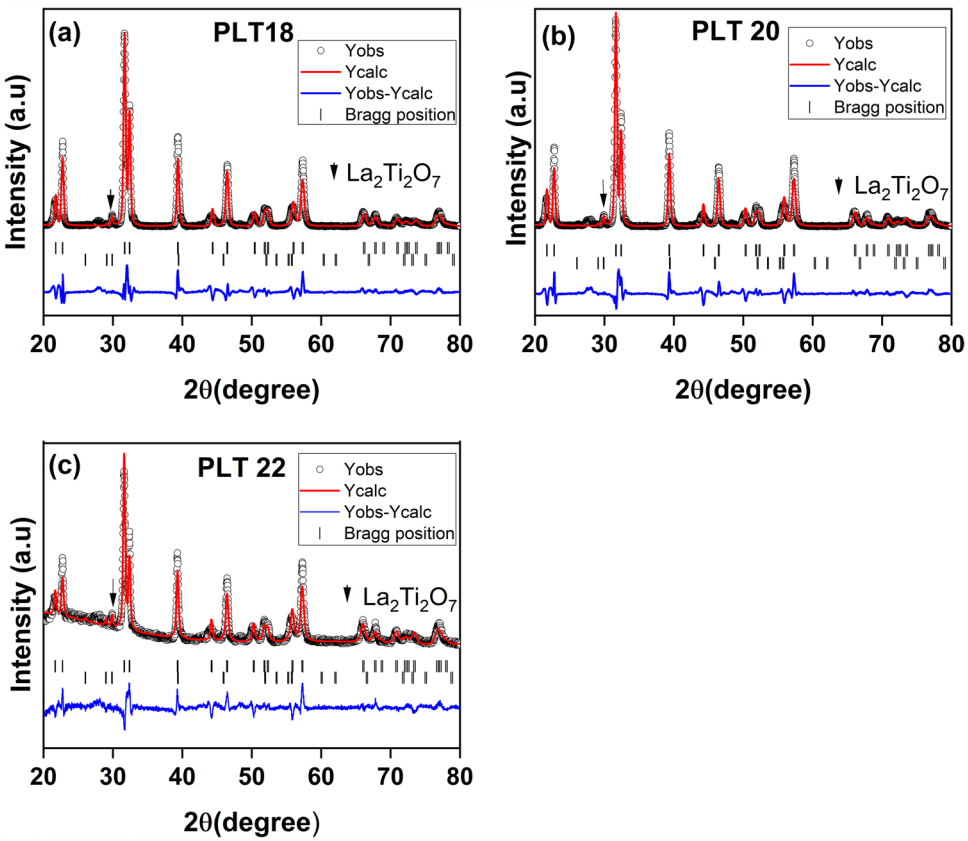

Fig. 4 Rietveld refinement of X-ray diffraction patterns for PLT ceramics (**a**) PLT18, (**b**) PLT20, and (**c**) PLT22. Open circles: observed intensities (Yobs); red line: calculated pattern (Ycalc); blue line: difference (Yobs–Ycalc); vertical ticks: Bragg peak positions. Arrows mark weak reflections from a minor $La_2Ti_2O_7$ secondary phase

Table 3 Structural parameters and Rietveld refinement results for PLT18, PLT20 and PLT22 ceramics

Ceramics	*a* (Å)	c (Å)	c/ *a* Ratio	%($La_2Ti_2O_7$)	R_{Bragg}	R_{wp}	R_f
PLT18	3.9089(2)	4.0982(3)	1.048	5.88	6.19	17.4	6.05
PLT20	3.9090(2)	4.0931(3)	1.047	6.47	7.79	22.1	4.83
PLT22	3.9101(3)	4.0840(3)	1.045	11.53	11.4	21.3	4.28

content and the presence of only trace amounts of $La_2Ti_2O_7$ (Table 3), both of which align with the microstructural reported previously.

Table 3 presents the structural parameters obtained from Rietveld refinement of X-ray diffraction data for PLT18, PLT20, and PLT22 ceramics sintered at their respective optimized temperatures and times and subsequently subjected to post-annealing. All samples crystallized in a tetragonal perovskite-type structure, consistent with previous reports for PLT ceramics. The refined lattice parameters show a gradual increase in *a* parameter and decrease in c with increasing lanthanum content, attributable to the smaller ionic radius of La^{3+} relative to Pb^{2+}, suggesting successful incorporation of La^{3+} into the A-site of the perovskite lattice [16, 17]. This trend is accompanied by a slight decrease in *c/a*, indicating a subtle doping-induced lattice distortion, corroborated by the evolution of transgranular fracture features and by the increased fraction of secondary phases with rising lanthanum content. However, a clear reduction of the secondary phase is evident in the densified specimens compared with the calcined powders. This behavior is typical of PbO-based ceramics and is consistent with the ceramic processing route adopted in this work, where densification was carried out using a sealed-crucible configuration specifically designed to suppress PbO volatilization (Fig. 1). In Pb-based perovskites, PbO loss is well known to drive non-stoichiometry and promote the formation of secondary phases, whereas PbO-controlled atmospheres (e.g., sealed crucibles and/or sacrificial powder beds) mitigate Pb deficiency and thereby suppress these phases. Furthermore, densification under PbO-controlled conditions, together with an adequate thermal budget (higher sintering temperature employed here), promotes perovskite formation at the expense of secondary phases. These effects support the observed decrease in $La_2Ti_2O_7$ in the densified ceramics relative to the calcined powders, as has also been reported by other authors [18, 19]. After densification, the PLT22 sample exhibited the highest fraction of secondary phases. This feature may be related to the grain-growth kinetics of these ceramics, although PLT22 was densified at a higher temperature and for a longer dwell time than PLT18 and PLT20 (Table 1), the increase in grain size was not abrupt. A plausible explanation is that secondary-phase particles induce grain-boundary pinning, which decreases boundary mobility and consequently suppresses grain coalescence during sintering.

The refinement quality indicators (R_{Bragg}, R_{wp}, and R_f) reported in Table 3 fall within acceptable ranges, confirming a good agreement between the experimental data and the calculated model.

Figure 5 presents the real permittivity (ε′) at 1 kHz as a function of temperature for PLT18, PLT20, and PLT22 ceramics sintered at their respective optimized temperatures and times and subsequently subjected to post-annealing. All ceramics display a marked anomaly associated with the ferroelectric-paraelectric phase transition. The maximum permittivity shifts towards lower temperatures with increasing lanthanum concentration, accompanied by peak broadening, similar behavior was found by other researchers [20]. This behavior reflects the progressive stabilization of a diffuse phase transition as La^{3+} is incorporated into the $PbTiO_3$ lattice. The observed dielectric response correlates well with the structural and microstructural data. The XRD refinements revealed a reduction in tetragonality (c/*a*) with increasing lanthanum content, consistent with the lowering of the transition temperature and the weakening of the ferroelectric distortion. Similarly, SEM analysis showed that the average grain size increases slightly from PLT18 to PLT22. Larger grains are known to enhance dielectric permittivity near the transition, while the increasing fraction of the $La_2Ti_2O_7$ secondary phase, identified by Rietveld refinement, contributes to peak broadening and increased dielectric losses. Altogether, the dielectric measurements confirm the interplay between crystal structure, grain size, and phase composition in determining the functional response of PLT ceramics obtained in this work.

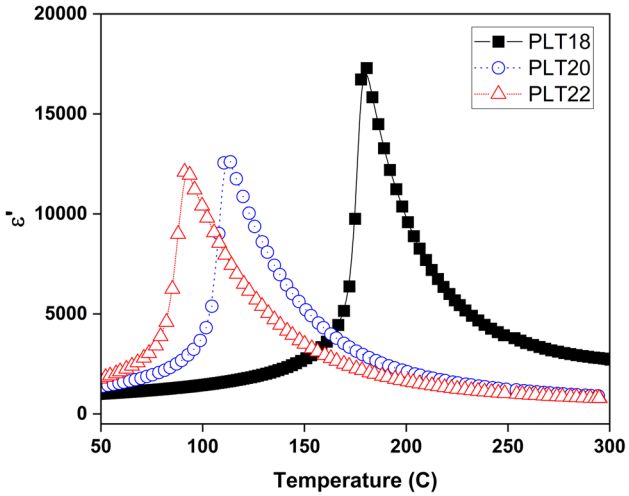

Fig. 5 Temperature dependence of the real, ε′ permittivity for PLT18, PLT20, and PLT22 ceramics at 1 kHz

The degree of the disorderness of the PLT for the samples was evaluated using the expression (2):

$$\left(\frac{1}{\varepsilon}-\frac{1}{\varepsilon_{max}}\right)=\frac{(T-Tc)^{\gamma}}{C} \tag{2}$$

where ε_{max} is maximum permittivity, γ is the major of diffuseness of the ferroelectric to paraelectric transition, C is the Curie constant and Tc is Curie temperature [21, 22]. The values of γ were estimated from the slope of the plot shown in Fig. 6 and are summarized in Table 4. The

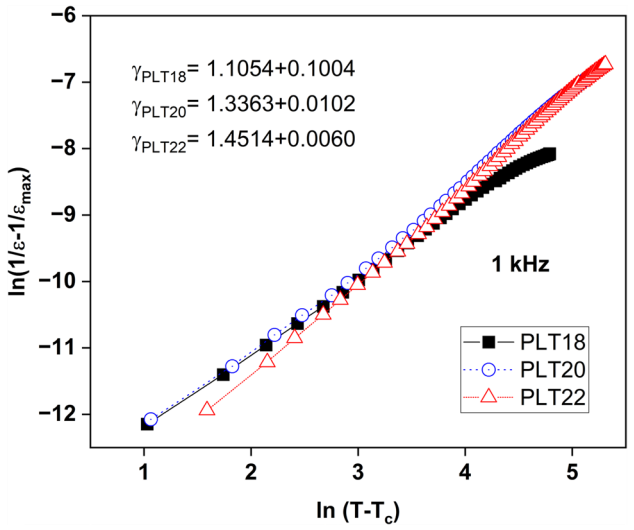

Fig. 6 Modified Curie–Weiss analysis for PLT ceramics obtained in this work

Table 4 Dielectric parameters and loss factors of densified PLT18, PLT20 and PLT22 ceramics

Densified Ceramic	Tc(°C)	ε′	ε″	γ	tanδ
PLT18	180(1)	17,289(5)	10(2)	1.1054 ± 0.0104	5.78×10^{-4}
PLT20	114(1)	12,604(5)	60(2)	1.3363 ± 0.0102	4.76×10^{-3}
PLT22	91(1)	12,101(5)	21(2)	1.4514 ± 0.0060	1.74×10^{-3}

γ parameter increases with increasing lanthanum content, confirming that the phase transition becomes progressively more diffuse as the lanthanum concentration rises [22]. This behavior is consistent with A-site La^{3+} substitution and charge-compensating defects, which introduce chemical/charge disorder and random fields, yielding a distribution of local Curie temperatures across and within grains [23]. Microstructurally, La^{3+} addition tends promotes defect/solute segregation at grain boundaries, leading to finer ferroelectric domains, enhanced domain-wall density and pinning, and increased internal stress heterogeneity altogether broadening the dielectric peak and raising γ as observed in this work.

Table 4 summarizes the dielectric response of the PLT18, PLT20, and PLT22 ceramics prepared in this work and reveals a clear trend: the Curie temperature decreases with increasing lanthanum concentration, consistent with the La^{3+}-induced reduction in tetragonality and, consequently, the weakening of long-range ferroelectric order. The maximum permittivity remains high but decreases with increasing lanthanum content, reflecting enhanced compositional disorder [24]. Concurrently, the diffuseness exponent (γ) increases, quantitatively evidencing a progressively more diffuse transition. Dielectric losses were generally low. However, as future work, we plan to perform transmission electron microscopy (TEM) and atomic force microscopy (AFM) studies to directly examine the evolution of ferroelectric domain structures as a function of lanthanum concentration.

Figure 7 shows the transmittance (at wavelength 650 nm) of PLT18, PLT20, and PLT22 ceramics obtained in this work. Inset: photograph of a representative PLT20 pellet illustrating its optical clarity. PLT20 exhibits the highest transmittance, whereas PLT18 and PLT22 show significantly lower values. The reduced transmittance in PLT18 may be attributed to smaller grain size, which increases the density of grain boundaries well-known light-scattering centers [25, 26]. In the case of PLT22, the lower transmittance can be related to the higher amount of secondary phases present, which can be corroborated by the results of Rietveld refinements. Such secondary-phase inclusions are expected to enhance diffuse scattering due to refractive-index/absorption contrast with the PLT matrix and scattering at particle–matrix interfaces, thereby reducing optical transmission.

The electro-optic response of the PLT18, PLT20, and PLT22 ceramics synthesized in this work is shown in Fig. 8. Both coefficients decrease with increasing lanthanum content. This trend mirrors the behavior of the maximum dielectric permittivity as a function of lanthanum concentration. The reduction in both coefficients with increasing La^{3+} suggests a weakening of the ferroelectric state—lower spontaneous polarization, reduced domain alignment/mobility, and diminished dielectric susceptibility—which suppresses the linear (Pockels) response and, to a lesser extent, the quadratic (Kerr) response. The electro-optic coefficients are of the same order as those used in

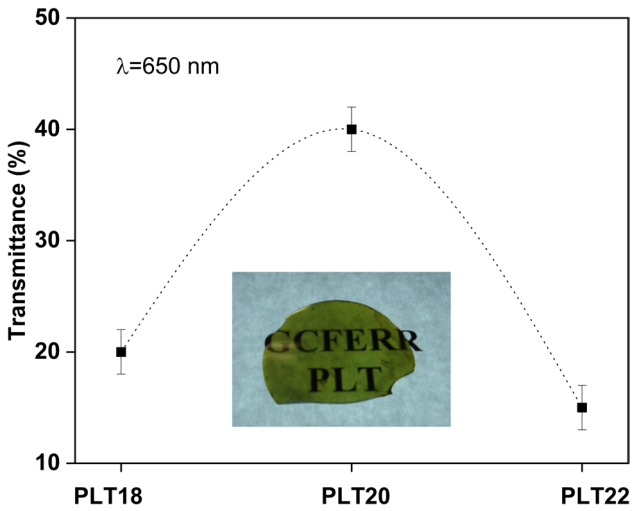

Fig. 7 Optical Transmittance at 650 nm for PLT18, PLT20, and PLT22 ceramics obtained in this work. The dotted line serves as a visual guide. Inset: Photograph of PLT20 ceramics demonstrating optical transparency

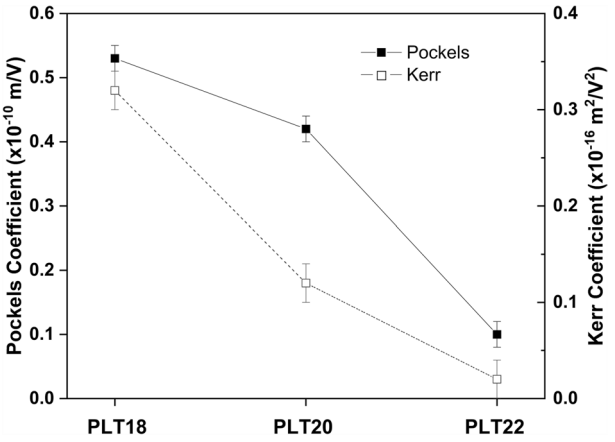

Fig. 8 Pockels and Kerr coefficients as a function of lanthanum concentration for PLT18, PLT20, and PLT22 ceramics synthesized in this work

electro-optic devices; however, further studies are required to improve the transmittance of the samples and to identify optimal conditions (e.g., frequency and temperature) for device applications.

4 Conclusion

This study demonstrates that a narrow lanthanum doping range ($0.18 \leq x \leq 0.22$) in $Pb_{1-x}La_xTiO_3$ ceramics yields a unique balance between structural relaxation, densification behavior, and functional performance. The structural changes induced by La^{3+} substitution are directly linked to enhanced dielectric and electro-optical properties, with $x = 0.20$ emerging as the optimal composition. These findings highlight the critical importance of compositional tuning and microstructural control in optimizing multifunctional perovskite ceramics.

A-site La^{3+} substitution preserves the tetragonal perovskite structure while reducing tetragonality, which correlates with a systematic decrease in Tc and a more diffuse ferroelectric–paraelectric transition. The Rietveld quality indicators denote satisfactory fits, supporting the structural trends derived from XRD.

PLT20 offers the best compromise between optical and dielectric performance and moderate loss making it the most promising candidate for transparent ferroelectric devices from $PbTiO_3$ doped with lanthanum.

The progressive increase in the diffuseness exponent (γ) with La^{3+} addition, together with the reduction in tetragonality indicates enhanced chemical/charge disorder. This microstructural evolution accounts for the broadened dielectric peak and the monotonic decrease of the Pockels/Kerr coefficients at higher lanthanum contents.

Acknowledgements This research was partially supported by Brazilian Agencies: CAPES, CNPq and FAPESP and Colombian Agencies: CODI, (Project 2022-52831 de la Universidad de Antioquia)

Author contribution Author Contributions F.L. and L.S. wrote the main manuscript text. F.L. prepared Figs. 1, 5, 6, 7, and 8. J.V.C. performed the Rietveld refinements and contributed to the analysis of the corresponding figures. L.S. prepared the remaining figures. D.G. and J.E. carried out the experimental measurements and contributed to the discussion of the results. All authors reviewed and approved the final manuscript.

Funding Open Access funding provided by Colombia Consortium

Data availability No datasets were generated or analysed during the current study.

Declarations

Competing interests The authors declare no competing interests.

References

1. N.P. Yadav, C. Joshi, P. Agnihotri, J.P. Nayak, R. Rai, J. Alloys Compd. (2025). https://doi.org/10.1016/j.jallcom.2025.180668
2. S. Jiang, Y. Wang, G. Zheng, Nanomaterials (2025). https://doi.org/10.3390/nano15020109
3. F.A. Londoño, J.A. Eiras, D. Garcia, Opt. Mater. **34**, 1310 (2012)
4. F.A. Londono, J.A. Eiras, D. Garcia, Bol. Soc. Esp. Ceram. Vidrio **51**, 353 (2012)
5. D. Hennings, G. Rosenstein, Mater. Res. Bull. **7**, 1505 (1972)
6. T. Yamamoto, H. Igarashi, K. Okazaki, J. Am. Ceram. Soc. **66**, 363 (1983)
7. I. Simecek, O. Marik, M. Jelinek, Romanian Journal of Information Science and Technology **18**, 182 (2015)
8. D. G. Fernando A. Londoño , Jose A. Eiras, Revista Latinoamericana de Metalurgia y Materiales **31**, 52 (2011).
9. G.S. Snow, J. Am. Ceram. Soc. **56**, 91 (1973)
10. A.R.C. Gerlt, A.K. Criner, L. Semiatin, E.J. Payton, J. Am. Ceram. Soc. **102**, 37 (2019)
11. L. Lutterotti, R. Ceccato, R. Dal Maschio, E. Pagani, Mater. Sci. Forum **278–281**, 87 (1998)
12. N. Sahu, S. Panigrahi, Bull. Mater. Sci. **34**, 1495 (2011)
13. L. Amarande, C. Miclea, C. Tanasoiu, J. Eur. Ceram. Soc. **22**, 1269 (2002)
14. T. Bongkarn, G. Rujijanagul, S.J. Milne, Mater. Lett. **59**, 1200 (2005)

15. J. P. Guha, D. J. Hong, and H. U. Anderson, Journal of the American Ceramic Society **71**, C (1988).
16. N. Sahu, S. Panigrahi, Ceram. Int. **38**, 1085 (2012)
17. U. Younas, M. Atif, A. Anjum, M. Nadeem, T. Ali, R. Shaheen, W. Khalid, Z. Ali, RSC Adv. **13**, 5293 (2023)
18. B.H. Chen, C.L. Huang, L. Wu, Solid-State Electron. **48**, 2293 (2004)
19. C. Miclea, C. Tanasoiu, C.F. Miclea, L. Amarande, A. Gheorghiu, I. Spanulescu, C. Plavitu, C.T. Miclea, M.C. Cioangher, L. Trupina, A. Iuga, J. Eur. Ceram. Soc. **27**, 4055 (2007)
20. P.P. Neves, A.C. Doriguetto, V.R. Mastelaro, L.P. Lopes, Y.P. Mascarenhas, A. Michalowicz, J.A. Eiras, J. Phys. Chem. B **108**, 14840 (2004)
21. P. Bharathi and K. B. R. Varma, Journal of Applied Physics **116**, (2014).
22. A.E. Sutherland, J. Am. Ceram. Soc. **73**, 3122 (1990)
23. V.V. Kirillov, V.A. Isupov, Ferroelectrics **5**, 3 (1973)
24. M. Mostafa, Z.A. Alrowaili, G.M. Rashwan, M.K. Gerges, Heliyon (2020). https://doi.org/10.1016/j.heliyon.2020.e03389
25. Y. Masuda, T. Tsukamoto, Ferroelectrics **172**, 243 (1995)
26. I. Milisavljevic, M. Zhang, Q. Jiang, Q. Liu, Y. Wu, J. Mater. (2025). https://doi.org/10.1016/j.jmat.2024.04.002